Centromere Dysfunction Compromises Mitotic Spindle Pole Integrity

Geneviève Almouzni, Raphaël Rodriguez, Renata Basto

Report

Current Biology

Centromere Dysfunction Compromises Mitotic Spindle Pole Integrity

Graphical Abstract

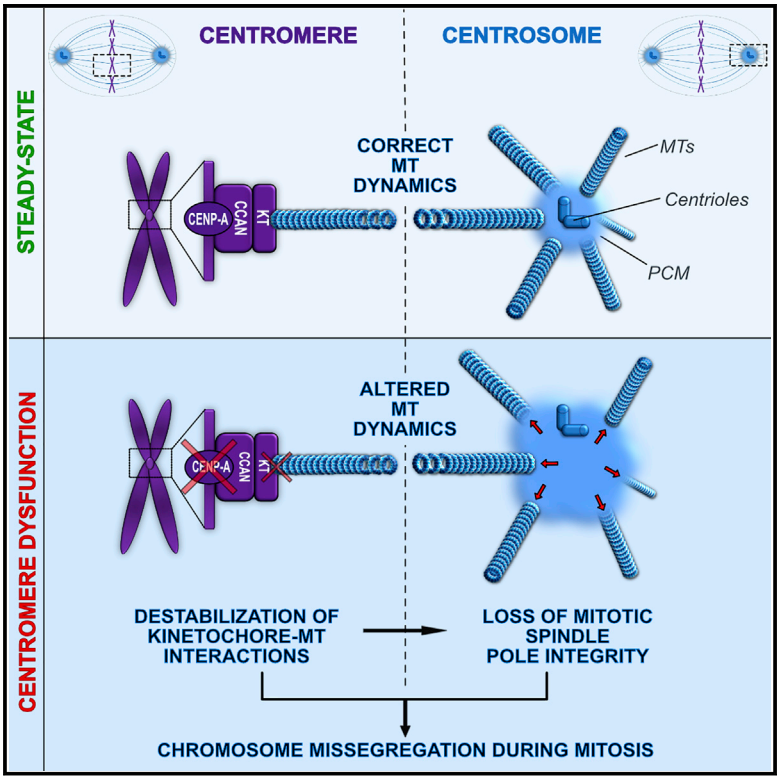

Highlights

- Centromere dysfunction leads to loss of mitotic spindle pole integrity
- This results from disruption of kinetochore-microtubule interactions
- Inducing microtubule stability restores spindle pole defects
- Spindle pole defects contribute to chromosome segregation errors

Authors

Simon Gemble, Anthony Simon, Carole Pennetier, ..., Geneviève Almouzni, Daniele Fachinetti, Renata Basto

Correspondence

daniele.fachinetti@curie.fr (D.F.), renata.basto@curie.fr (R.B.)

In Brief

Gemble et al. show that in human cells, centromere dysfunction results in microtubule minus-end relocalization and PCM dispersion during mitosis. This loss of mitotic spindle pole integrity is dependent on altered microtubule dynamics and contributes to chromosome segregation errors resulting from centromere dysfunction.

Gemble et al., 2019, Current Biology 29, 1–9
September 23, 2019
https://doi.org/10.1016/j.cub.2019.07.052

CellPress

Please cite this article in press as: Gemble et al., Centromere Dysfunction Compromises Mitotic Spindle Pole Integrity, Current Biology (2019), https://doi.org/10.1016/j.cub.2019.07.052

Current Biology
Report

Centromere Dysfunction Compromises Mitotic Spindle Pole Integrity

Simon Gemble,[1,2] Anthony Simon,[1] Carole Pennetier,[1] Marie Dumont,[2] Solène Hervé,[2] Franz Meitinger,[3] Karen Oegema,[3] Raphaël Rodriguez,[4] Geneviève Almouzni,[5] Daniele Fachinetti,[2,*] and Renata Basto[1,6,*]
[1]Institut Curie, PSL Research University, CNRS, UMR144, Biology of centrosomes and genetic instability lab, 75005 Paris, France
[2]Institut Curie, PSL Research University, CNRS, UMR144, Molecular Mechanisms of Chromosome Dynamics lab, 75005 Paris, France
[3]Department of Cellular and Molecular Medicine, Ludwig Institute for Cancer Research, University of California, San Diego, La Jolla, CA 92093-0670, USA
[4]Institut Curie, PSL Research University, CNRS, UMR366/U1143, Chemical Biology of Cancer lab, 75005 Paris, France
[5]Institut Curie, PSL Research University, CNRS, UMR3664, Chromatin Dynamics lab, 75005 Paris, France
[6]Lead Contact
*Correspondence: daniele.fachinetti@curie.fr (D.F.), renata.basto@curie.fr (R.B.)
https://doi.org/10.1016/j.cub.2019.07.052

SUMMARY

Centromeres and centrosomes are crucial mitotic players. Centromeres are unique chromosomal sites characterized by the presence of the histone H3-variant centromere protein A (CENP-A) [1]. CENP-A recruits the majority of centromere components, collectively named the constitutive centromere associated network (CCAN) [2]. The CCAN is necessary for kinetochore assembly, a multiprotein complex that attaches spindle microtubules (MTs) and is required for chromosome segregation [3]. In most animal cells, the dominant site for MT nucleation in mitosis are the centrosomes, which are composed of two centrioles, surrounded by a protein-rich matrix of electron-dense pericentriolar material (PCM) [4]. The PCM is the site of MT nucleation during mitosis [5]. Even if centromeres and centrosomes are connected via MTs in mitosis, it is not known whether defects in either one of the two structures have an impact on the function of the other. Here, using high-resolution microscopy combined with rapid removal of CENP-A in human cells, we found that perturbation of centromere function impacts mitotic spindle pole integrity. This includes release of MT minus-ends from the centrosome, leading to PCM dispersion and centriole mis-positioning at the spindle poles. Mechanistically, we show that these defects result from abnormal spindle MT dynamics due to defective kinetochore-MT attachments. Importantly, restoring mitotic spindle pole integrity following centromere inactivation lead to a decrease in the frequency of chromosome mis-segregation. Overall, our work identifies an unexpected relationship between centromeres and maintenance of the mitotic pole integrity necessary to ensure mitotic accuracy and thus to maintain genetic stability.

RESULTS AND DISCUSSION

Centromere Dysfunction Impacts the Integrity of the Mitotic Spindle Pole

To investigate the consequences of centromere dysfunction during mitosis, we studied the consequences of rapid centromere protein A (CENP-A) depletion using the AID system (referred to as CENP-A^{AID}) in diploid non-transformed human RPE-1 cells (Figures 1A and 1B). CENP-A depletion for short periods of time results in a slight decrease in centromere and kinetochore components without impairing chromosome segregation [6]. In contrast, CENP-A loss for one entire cell cycle leads to a severe degree of kinetochore perturbation and higher rates of chromosome segregation errors (Figures S1A and S1B) [6–8].

Using high-resolution microscopy (HRM), we characterized mitotic spindle poles following centromere dysfunction. Under these conditions, the area occupied by the spindle poles and the microtubule (MT) minus-end components NuMA and ASPM [9] increased (Figures 1C, 1D, and S1C–S1E). Further, the PCM components CEP192, CEP215, and γ-tubulin appeared dispersed around the spindle poles (Figures 1C, 1E, 1F, and S1F–S1H). PCM dispersion in response to CENP-A depletion was mitosis specific (from prometaphase to anaphase) (Figures S1I and S1J), and it was observed also in other cell lines (Figures S1K and S1L). While MT minus-end re-localization was noticed at early time points (1 h of Auxin, Figure 1D), PCM dispersion was only detected after 10 h of Auxin addition (Figures 1E and 1F). We also observed pairs of centrioles that, despite being always together (Figure S1M), were mis-positioned at the center of the spindle pole (hereafter called displaced centrioles). Mis-position was defined by the increase in the angle formed between the pole-to-pole axis and the centrioles (angle α, Figures 1G–1I), which was increased in CENP-A-depleted cells (Figures 1G–1I). Importantly, using the association Fisher's exact test, we found a significant association between all these defects (Figures 1J and 1K). PCM dispersion was restricted to the NuMA area. It is thus possible that MT minus-end mis-positioning occurs first leading then to PCM dispersion and displaced centrioles.

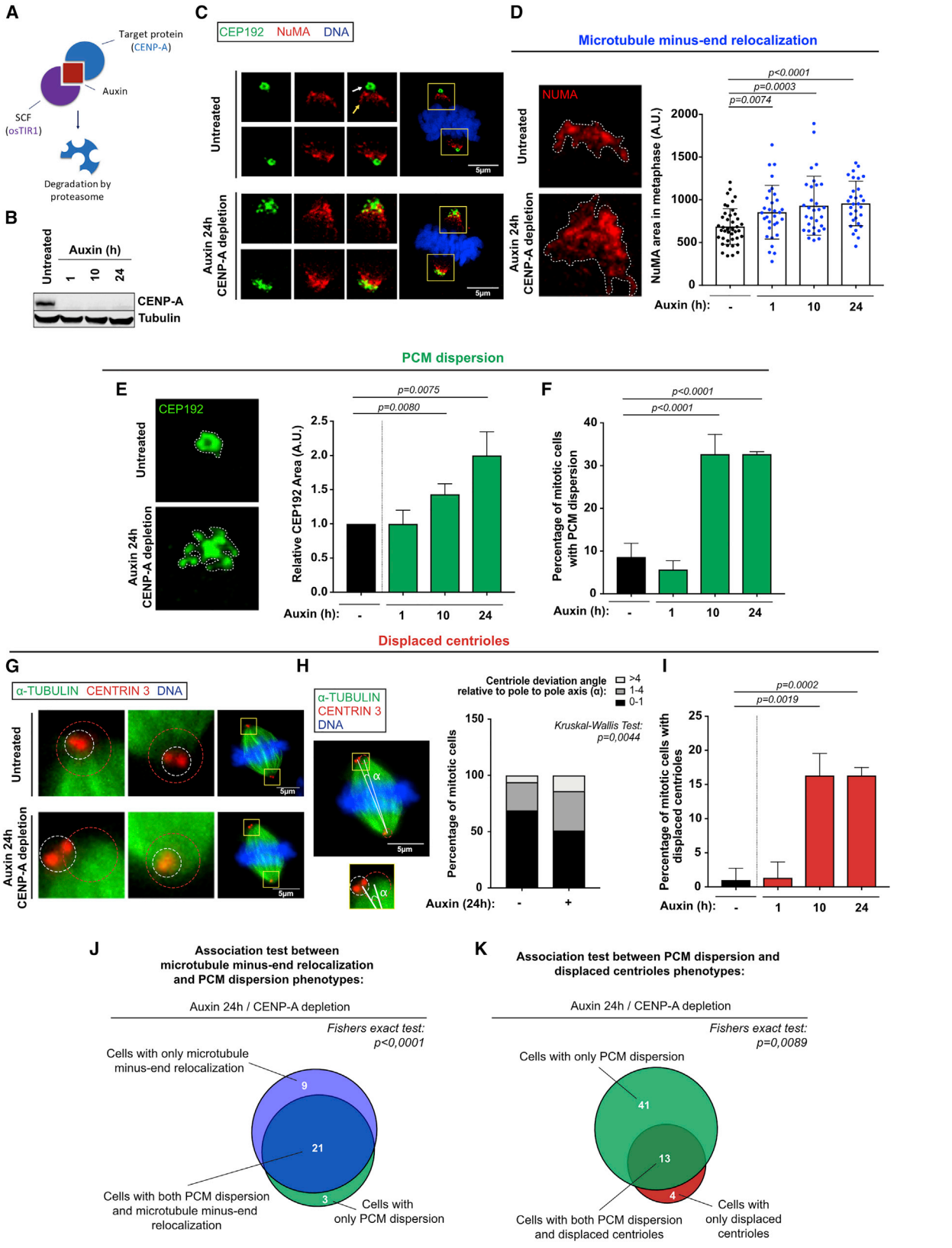

(legend on next page)

Destabilization of Kinetochore-MT Interactions Is Sufficient to Promote Loss of Mitotic Pole Integrity

CENP-C and NDC80 levels are reduced in CENP-A-depleted cells [6]. Interfering with these components results in spindle pole integrity defects (Figures 2A, S2A, and S2B), suggesting that perturbing kinetochores and MT attachments (K-MTA) is sufficient to compromise pole integrity, even in the presence of CENP-A. We next used TAI-1, an NDC80 inhibitor that destabilizes the interaction between NDC80 and MTs, without affecting centromere architecture [10]. Increasing concentrations of TAI-1 caused a dose-dependent increase in mitotic errors (Figure S2D). To mimic the partial impairment of K-MTAs observed upon acute CENP-A depletion (Figure S1B and [6]), we treated cells with low doses of TAI-1. NDC80 inhibition over time resulted in a significant increase in the number of mitotic cells displaying misaligned chromosomes and spindle pole defects (Figures 2F–2K and S2E–S2G). We ruled out an effect of NDC80 depletion in CENP-A localization or maintenance (Figure S2H) or an additive effect between CENP-A depletion and TAI-1 (Figures S2I and S2J). Together with data from [6], we concluded that even minor K-MTA perturbations are sufficient to trigger loss of spindle pole integrity.

We assessed the dynamics of PCM dispersion by following GFP-CEP192 by time-lapse microscopy. In control cells, CEP192 accumulates at the centrosome until metaphase and is then progressively unloaded. Although GFP-CEP192 fluorescence intensity was increased after TAI-1 treatment, we noticed that CEP192 spread away from the centrosome before metaphase (Figure 2L and supplementary Video S1). This occurred within the time span of normal mitosis (~17 min after NEBD; Figure 2L).

Perturbing K-MTAs activates the spindle assembly checkpoint (SAC) and extends mitotic duration (ExMD) that can result in cohesion fatigue and spindle pole defects like centrosome fragmentation and multipolar spindles [11, 12]. We never observed this type of defects and ruled out an effect of CENP-A depletion in cohesion fatigue (Figures S2K and S2L). To test whether ExMD contributes to loss of mitotic spindle pole integrity, we used two strategies that result in ExMD by ~20–30 min, similarly to what was observed in CENP-A-depleted cells [6]. Both treatment with Apcin—a chemical inhibitor of the APC/C [13]—and Cyclin B1 siRNA [14] (Figures S2M–S2O) did not cause spindle pole defects (Figures S2P and S2Q). Accordingly, treatment with MPI-0479605—a chemical inhibitor of MPS1—reduced mitotic duration in CENP-A-depleted cells (Figure S2R) but did not suppress PCM dispersion (Figure S2S). In conclusion, ExMD does not contribute to loss of pole integrity upon centromere dysfunction.

PCM Dispersion Occurs by an MT Dynamics-Dependent Mechanism

The NDC80 complex stabilizes MTs *in vitro* and *in vivo* [15, 16]. We tested whether CENP-A depletion leads to MT destabilization through defects in maintaining NDC80-mediated K-MTAs. To investigate this possibility, we first subjected cells to mild cold treatment, which is known to induce MT depolymerization of most spindle MTs, with the exception of the kinetochore fibers (K-MTs) [17]. Upon centromere dysfunction, a drastic reduction in the number of K-MTs was observed (Figures 3A, 3B, and S3A). To confirm the perturbation of MT dynamics, we measured the length of GFP-EB1 tracks, a marker of MT plus-ends [9], as a readout of MT growth [18]. Either CENP-A depletion or NDC80 inhibition led to a decrease in the length of EB1 tracks (Figure 3C; Video S2; Figures S3B and S3C). These results demonstrate that centromere dysfunction and the subsequent reduction in kinetochore NDC80 levels decrease MT stability and dynamics.

Our results suggest that loss of pole integrity results from defects in MT stability following centromere dysfunction. To test this hypothesis, we treated cells with Taxol, an MT-stabilizing agent [19] that binds β-tubulin monomers [20] along the entire MT length [21]. This was sufficient to fully prevent PCM dispersion upon centromere dysfunction (Figures 3D, 3E, and S3D–S3F). Similarly, decreasing the levels of MCAK—an MT depolymerase kinesin [22]—to induce MT stabilization [23, 24] was sufficient to rescue spindle pole defects upon centromere dysfunction (Figures 3F–3H and S3G–S3J).

We also inhibited MT minus-end dynamics by depleting Katanin, a protein required to release MT minus-ends from the centrosome [25–27]. Using Katanin siRNA, we observed that spindle pole defects were decreased upon centromere dysfunction (Figures 3I–3K and S3K). Thus, MT release from the centrosome occurs in a Katanin-dependent manner most likely

Figure 1. Centromere Dysfunction Compromises Mitotic Pole Integrity

(A) Schematic representation of the auxin inducible degron (AID) system.

(B) CENP-A and α-Tubulin levels assessed by immunoblotting of cell lysates at the indicated time points.

(C) Super resolution microscopy (SRM) images showing NuMA (red), CEP192 (green) and DNA (blue). The yellow squares correspond to higher magnifications (HMs) shown on the left.

(D) Left panel: HM images of (C). Right panel: measurements of NuMA area at the indicated time points. Error bars represent means (EBRM) ± SD from 2 independent experiments (IEs) (>30 mitotic poles).

(E) Left panel: HMs of (C). Right panel: relative CEP192 area for the indicated time points. EBRM ± SD from 3 IEs (>65 cells).

(F) Percentage of cells with PCM dispersion. EBRM ± SD from 3 IEs (>50 cells).

(G) Immunofluorescence images of mitotic spindles (green), centrioles (red), and DNA (blue). The yellow squares correspond to HM on the left. The red and white circles label the spindle pole and centrioles respectively.

(H) Left panel: HM of (G). Right panel: percentage of cells in each angle (α) category. EBRM ± SD from 3 IEs (>70 cells). Statistical significance was assessed (SSA) using Kruskal-Wallis test.

(I) Percentage of cells showing displaced centrioles. EBRM ± SD from 3 IEs (>70 cells).

(J and K) Venn diagrams of cells with the indicated phenotypes. Statistical association between each phenotype was measured using Fisher's exact test. SSA with unpaired t tests.

Scale bars, 5 μm. See also Figure S1.

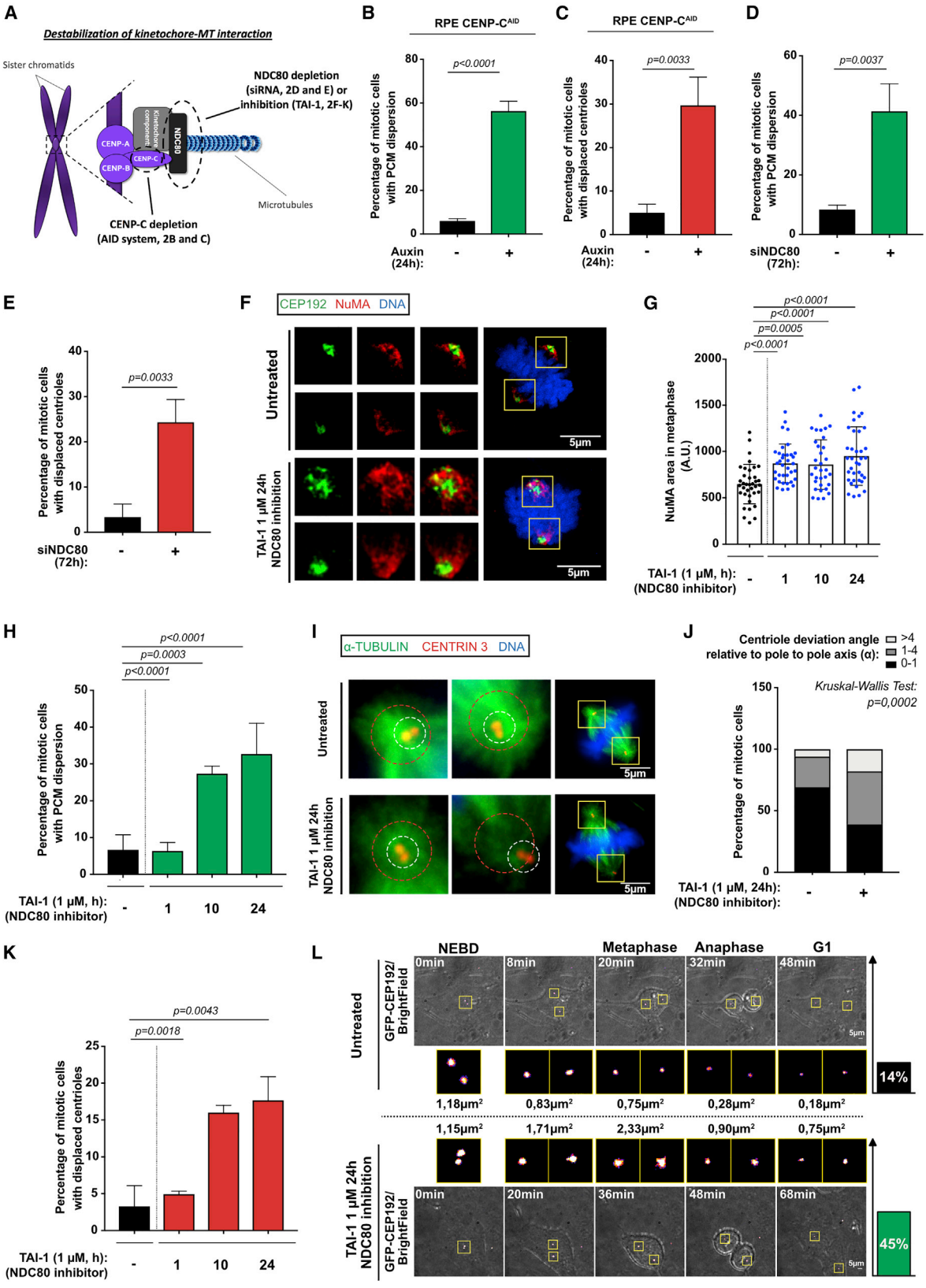

(legend on next page)

contributing to the outward spread of PCM proteins to the new MT minus-end localization.

Spindle Pole Defects Contribute to Chromosome Mis-Segregation Errors

We tested whether defects in pole integrity described here contributed to chromosome mis-segregation errors, typical of cells with centromere dysfunction (Figures S1A and S1B and [6]). Importantly, MT stabilization via MCAK or Katanin depletions did not decrease the percentage of unattached kinetochores upon centromere dysfunction (Figures 4A and S4E) but partially rescued the percentage of cells with mitotic defects (Figures 4B–4E and S4A–S4G) both in fixed or live cell-imaging experiments (Figures 4B–4G and S4A–S4H; Video S3). This rescue was not due to a slight increase in mitotic duration following Katanin and MCAK depletion (Figure S4I), as Apcin treatment did not restore proper chromosome segregation of CENP-A-depleted cells (Figure S4J). Altogether, these results suggest that in cells with compromised centromere function, stabilizing MTs and restoring pole integrity partially contribute to the amending of chromosome segregation errors by promoting chromosome alignment before anaphase onset.

Our findings are consistent with the model presented in Figure 4H. Overall, our work puts forward a novel functional interdependency between centromeres and centrosomes during mitosis: perturbing centromere function compromises mitotic pole integrity in an MT-dependent manner. Importantly, this type of defect was only detected after extended periods of CENP-A depletion (10–24 h), which is consistent with the observations that CENP-A depletion during G1 phase increased substantially the rate of chromosome mis-segregation in the following mitosis [6]. The means by which PCM dispersion, caused by centromere dysfunction, contributes to mitotic defects remain to be identified. It is possible that lack of spindle pole integrity stabilizes the position of polar chromosomes, which are then positioned away from the main chromosome mass. Alternatively, defects in spindle pole integrity might affect the interaction of polar MTs with chromosomes, compromising congression of misaligned chromosomes. In any case, these mis-localized chromosomes would skip the opportunity to be incorporated into the main daughter nuclei and form MN.

This surprising impact of centromere dysfunction on centrosome integrity offers new perspectives on the idea initially proposed by D. Mazia [28] on the coordination between the chromosome cycle with centrosomes and possibly other distant organelles even if in distinct compartments.

STAR★METHODS

Detailed methods are provided in the online version of this paper and include the following:

- KEY RESOURCES TABLE
- LEAD CONTACT AND MATERIAL AVAILABILITY
- EXPERIMENTAL MODEL AND SUBJECT DETAILS
  - Cell culture, generation of cell lines and treatments
- METHOD DETAILS
  - Immunofluorescence microscopy
  - Live imaging
  - Cold treatment
  - siRNA transfection
  - Western Blot analysis and antibodies
  - Chromosome spreads for cohesion defect analysis
- QUANTIFICATION AND STATISTICAL ANALYSIS
  - Quantifications
  - Statistical analysis
- DATA AND CODE AVAILABILITY

SUPPLEMENTAL INFORMATION

Supplemental Information can be found online at https://doi.org/10.1016/j.cub.2019.07.052.

ACKNOWLEDGMENTS

This work was supported by a PIC3i grant from the Institut Curie and the CNRS. The authors acknowledge the NIC at Institut Curie, the PICT-IBiSA. and FBI ANR10-INBS-04. F.M. and K.O. are funded by GSF ME 4713/1-1 and NIH grant GM074207. We thank the Fachinetti and Basto lab members, C. Bartocci and J. Pines, for helpful discussions and/or comments on the manuscript. The Fachinetti and Basto labs are members of the Labex CelTisPhyBio in PSL.

AUTHOR CONTRIBUTIONS

S.G. conceived the project, performed the large majority of the experiments, participated in their design, data analysis, and interpretation, generated the figures, and wrote the manuscript. A.S. performed and analyzed certain experiments. C.P. generated tools and S.H. generated cell lines and performed certain immunoblots. M.D. performed and analyzed metaphase spreads.

Figure 2. Destabilization of Kinetochore-MT Interactions Is Sufficient to Promote Loss of Mitotic Spindle Pole Integrity

(A) Schematic representation of centromere-kinetochore complexes and the strategies used to destabilize kinetochore-MT interactions.

(B–E) Percentage of cells in each category. EBRM ± SD from 3 IEs (>105 and >75 cells for B and C) (>50 and >60 cells for D and E).

(F) SRM images of CEP192 (green) and NuMA (red). DNA in blue. The yellow squares correspond to HMs shown on the left.

(G) NuMA area. EBRMs ± SD from 2 IEs (>35 mitotic poles).

(H) Percentage of cells with PCM dispersion. EBRMs ± SD from 3 IEs (>60 cells).

(I) Images of mitotic spindles (green), centrioles (red), and DNA in blue. The yellow squares correspond to HMs on the left. The red and white circles label the spindle pole and centrioles, respectively.

(J) Percentage of cells displaying the angle (α) indicated. EBRM ± SD from 3 IEs (>60 cells).

(K) Percentage of cells EBRM ± SD from 3 IEs (>60 metaphase cells).

(L) Stills of time-lapse of GFP-CEP192 cells. Time is in minutes. The yellow squares correspond to HMs on the central panel. Average CEP192 areas are indicated next to the images, and percentage of cells presenting PCM dispersion is indicated on the right. SSA with unpaired t tests was used for all figures, with exception of (J) and (L), which used Kruskal-Wallis test.

Scale bars, 5 μm. See also Figure S2 and Video S1

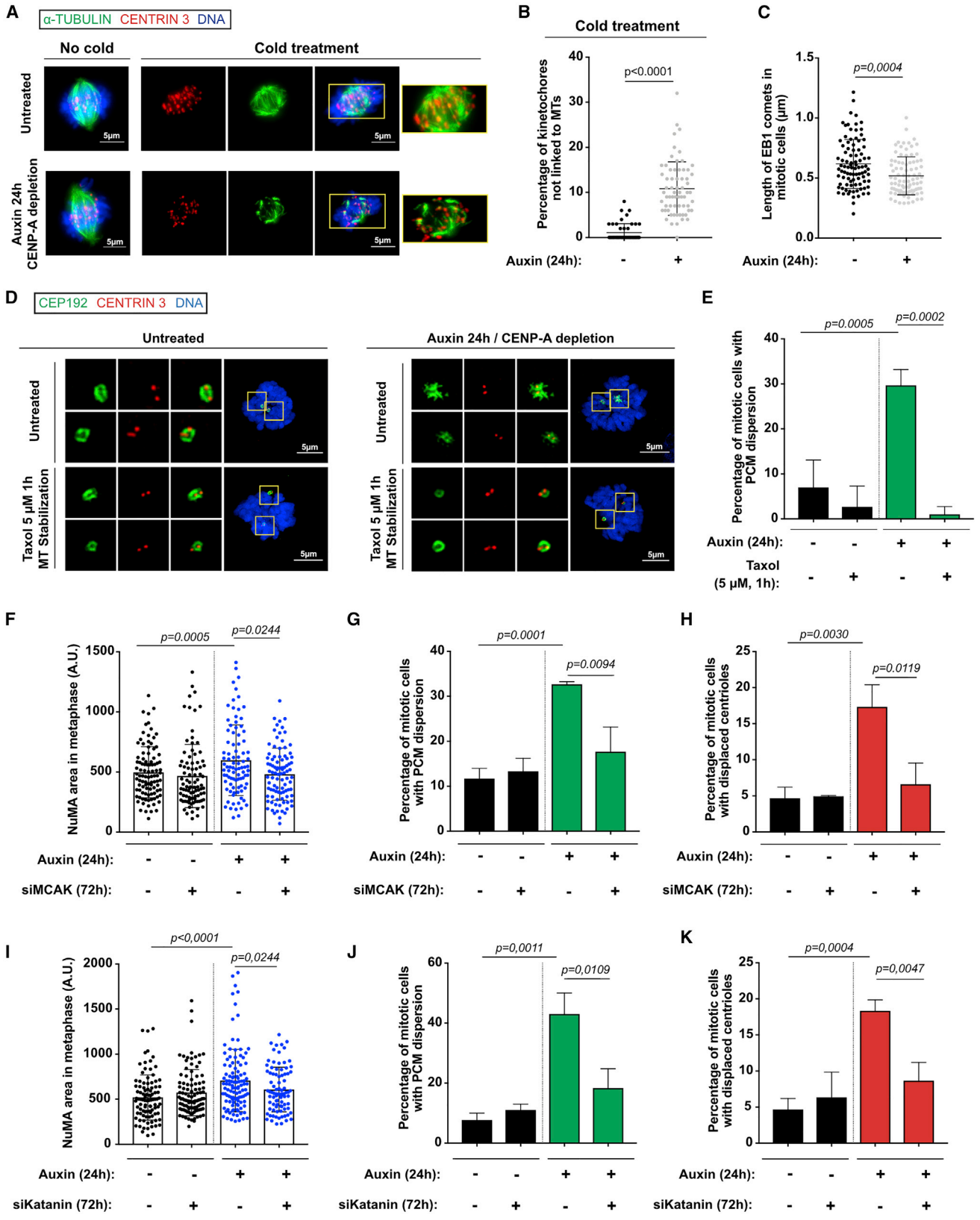

(legend on next page)

F.M. and K.O. generated GFP-CEP192 RPE-1 cell line. G.A. and R.R. contributed with the project conceptual framework. D.F. and R.B. discussed the results, interpreted the data, edited the manuscript, and supervised the project.

DECLARATION OF INTERESTS

The authors have no competing interests.

Received: November 7, 2018
Revised: June 21, 2019
Accepted: July 17, 2019
Published: September 5, 2019

REFERENCES

1. Earnshaw, W.C., and Rothfield, N. (1985). Identification of a family of human centromere proteins using autoimmune sera from patients with scleroderma. Chromosoma *91*, 313–321.
2. Fukagawa, T., and Earnshaw, W.C. (2014). The centromere: chromatin foundation for the kinetochore machinery. Dev. Cell *30*, 496–508.
3. Musacchio, A., and Desai, A. (2017). A molecular view of kinetochore assembly and function. Biology (Basel) *6*, E5.
4. Prosser, S.L., and Pelletier, L. (2017). Mitotic spindle assembly in animal cells: a fine balancing act. Nat. Rev. Mol. Cell Biol. *18*, 187–201.
5. Kollman, J.M., Merdes, A., Mourey, L., and Agard, D.A. (2011). Microtubule nucleation by γ-tubulin complexes. Nat. Rev. Mol. Cell Biol. *12*, 709–721.
6. Hoffmann, S., Dumont, M., Barra, V., Ly, P., Nechemia-Arbely, Y., McMahon, M.A., Hervé, S., Cleveland, D.W., and Fachinetti, D. (2016). CENP-A is dispensable for mitotic centromere function after initial centromere/kinetochore assembly. Cell Rep. *17*, 2394–2404.
7. Fachinetti, D., Folco, H.D., Nechemia-Arbely, Y., Valente, L.P., Nguyen, K., Wong, A.J., Zhu, Q., Holland, A.J., Desai, A., Jansen, L.E., and Cleveland, D.W. (2013). A two-step mechanism for epigenetic specification of centromere identity and function. Nat. Cell Biol. *15*, 1056–1066.
8. Régnier, V., Vagnarelli, P., Fukagawa, T., Zerjal, T., Burns, E., Trouche, D., Earnshaw, W., and Brown, W. (2005). CENP-A is required for accurate chromosome segregation and sustained kinetochore association of BubR1. Mol. Cell. Biol. *25*, 3967–3981.
9. Martin, M., and Akhmanova, A. (2018). Coming into focus: mechanisms of microtubule minus-end organization. Trends Cell Biol. *28*, 574–588.
10. Huang, L.Y., Lee, Y.S., Huang, J.J., Chang, C.C., Chang, J.M., Chuang, S.H., Kao, K.J., Tsai, Y.J., Tsai, P.Y., Liu, C.W., et al. (2014). Characterization of the biological activity of a potent small molecule Hec1 inhibitor TAI-1. J. Exp. Clin. Cancer Res. *33*, 6.
11. Karki, M., Keyhaninejad, N., and Shuster, C.B. (2017). Precocious centriole disengagement and centrosome fragmentation induced by mitotic delay. Nat. Commun. *8*, 15803.
12. Stevens, D., Gassmann, R., Oegema, K., and Desai, A. (2011). Uncoordinated loss of chromatid cohesion is a common outcome of extended metaphase arrest. PLoS ONE *6*, e22969.
13. Wang, L., Zhang, J., Wan, L., Zhou, X., Wang, Z., and Wei, W. (2015). Targeting Cdc20 as a novel cancer therapeutic strategy. Pharmacol. Ther. *151*, 141–151.
14. Soni, D.V., Sramkoski, R.M., Lam, M., Stefan, T., and Jacobberger, J.W. (2008). Cyclin B1 is rate limiting but not essential for mitotic entry and progression in mammalian somatic cells. Cell Cycle *7*, 1285–1300.
15. Umbreit, N.T., Gestaut, D.R., Tien, J.F., Vollmar, B.S., Gonen, T., Asbury, C.L., and Davis, T.N. (2012). The Ndc80 kinetochore complex directly modulates microtubule dynamics. Proc. Natl. Acad. Sci. USA *109*, 16113–16118.
16. Foley, E.A., and Kapoor, T.M. (2013). Microtubule attachment and spindle assembly checkpoint signalling at the kinetochore. Nat. Rev. Mol. Cell Biol. *14*, 25–37.
17. Eichenlaub-Ritter, U., and Ruthmann, A. (1982). Evidence for three "classes" of microtubules in the interpolar space of the mitotic micronucleus of a ciliate and the participation of the nuclear envelope in conferring stability to microtubules. Chromosoma *85*, 687–706.
18. Piehl, M., and Cassimeris, L. (2003). Organization and dynamics of growing microtubule plus ends during early mitosis. Mol. Biol. Cell *14*, 916–925.
19. Schiff, P.B., Fant, J., and Horwitz, S.B. (1979). Promotion of microtubule assembly in vitro by taxol. Nature *277*, 665–667.
20. Yang, C.H., and Horwitz, S.B. (2017). Taxol®: the first microtubule stabilizing agent. Int. J. Mol. Sci. *18*, E1733.
21. Pineda, J.J., Miller, M.A., Song, Y., Kuhn, H., Mikula, H., Tallapragada, N., Weissleder, R., and Mitchison, T.J. (2018). Site occupancy calibration of taxane pharmacology in live cells and tissues. Proc. Natl. Acad. Sci. USA *115*, E11406–E11414.
22. Desai, A., Verma, S., Mitchison, T.J., and Walczak, C.E. (1999). Kin I kinesins are microtubule-destabilizing enzymes. Cell *96*, 69–78.
23. Rankin, K.E., and Wordeman, L. (2010). Long astral microtubules uncouple mitotic spindles from the cytokinetic furrow. J. Cell Biol. *190*, 35–43.
24. Rizk, R.S., Bohannon, K.P., Wetzel, L.A., Powers, J., Shaw, S.L., and Walczak, C.E. (2009). MCAK and paclitaxel have differential effects on spindle microtubule organization and dynamics. Mol. Biol. Cell *20*, 1639–1651.
25. Dong, C., Xu, H., Zhang, R., Tanaka, N., Takeichi, M., and Meng, W. (2017). CAMSAP3 accumulates in the pericentrosomal area and accompanies microtubule release from the centrosome via katanin. J. Cell Sci. *130*, 1709–1715.
26. Ahmad, F.J., Yu, W., McNally, F.J., and Baas, P.W. (1999). An essential role for katanin in severing microtubules in the neuron. J. Cell Biol. *145*, 305–315.
27. Jiang, K., Faltova, L., Hua, S., Capitani, G., Prota, A.E., Landgraf, C., Volkmer, R., Kammerer, R.A., Steinmetz, M.O., and Akhmanova, A. (2018). Structural basis of formation of the microtubule minus-end-regulating CAMSAP-katanin complex. Structure *26*, 375–382.e4.
28. Mazia, D. (1987). The chromosome cycle and the centrosome cycle in the mitotic cycle. Int. Rev. Cytol. *100*, 49–92.
29. Vargas-Hurtado, S., Brault, J., Piolot, T., Leconte, L., Da Silva, N., Pennetier, C., Baffet, A., Marthiens, V., and Basto, R. (2019). Different mitotic spindle architectures influence mitotic accuracy during mammalian

Figure 3. PCM Dispersion Occurs by an MT Dynamics-Dependent Mechanism

(A) SRM images of mitotic spindles (green), centromeres (red), and DNA (blue) with the indicated treatments. The yellow squares correspond to HMs on the right.
(B and C) Percentage of kinetochores not attached to MTs (B) and the length of EB1 tracks (C). EBRM ± SD from 3 IEs (>50 cells and >85 EB1 tracks analyzed).
(D) SRM images of CEP192 (green), centrioles (red), and DNA (blue) after the indicated treatments. The yellow squares correspond to HMs on the left.
(E) Percentage of cells with PCM dispersion after the indicated treatments. EBRM ± SD from 3 IEs (>60 cells).
(F) NuMA area in cells transfected with the indicated siRNA. EBRM ± SD from 2 IEs (>85 mitotic poles).
(G and H) Percentage of cells after the indicated treatment. EBRM ± SD from 3 IEs (>60 cells).
(I) NuMA area after the indicated treatment. EBRM ± SD from 3 IEs (>85 mitotic poles).
(J and K) Percentage of mitotic cells in each category. EBRM ± SD from 3 IEs (>100 cells). SSA with unpaired t tests.
Scale bars, 5 μm. See also Figure S3 and Video S2.

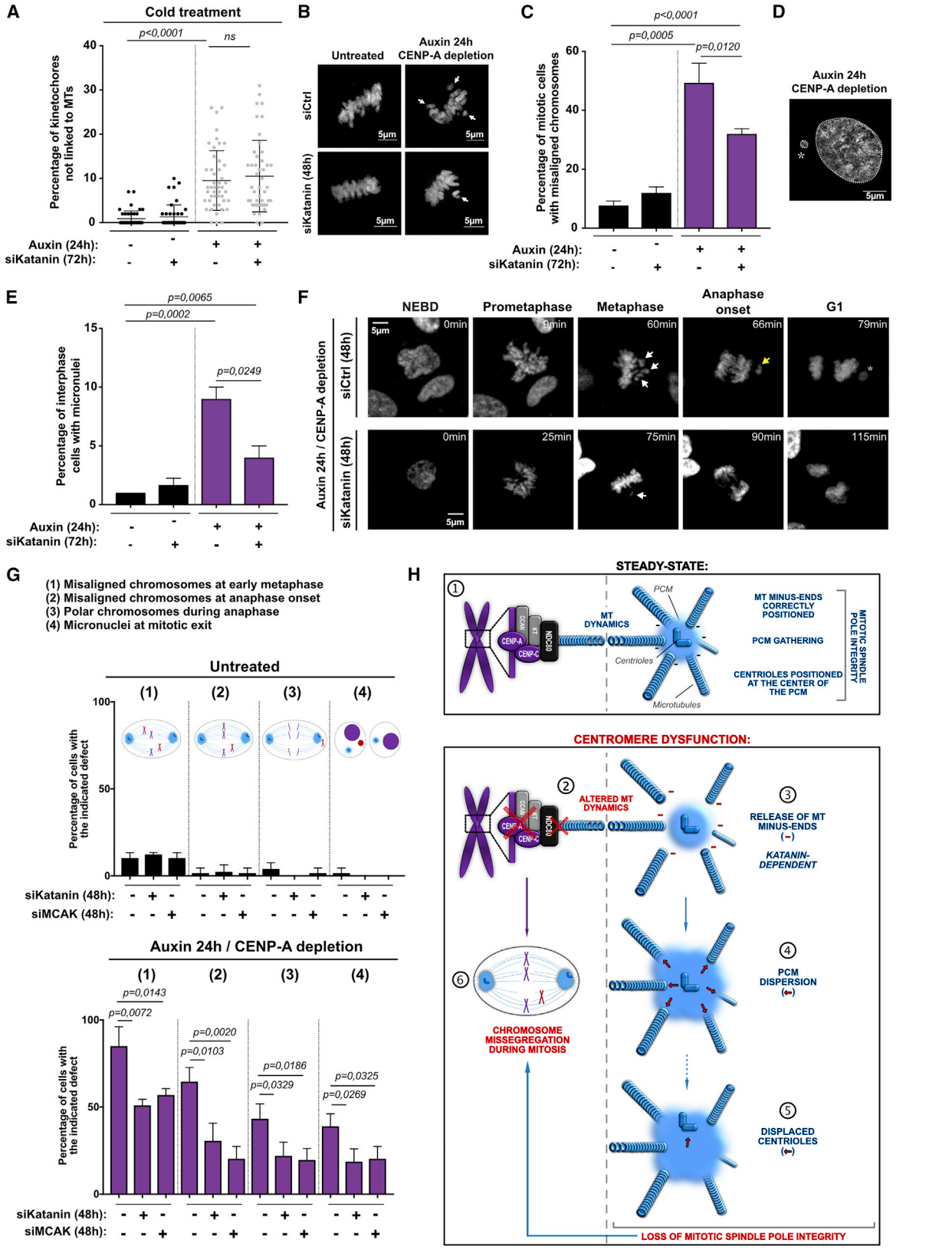

(legend on next page)

brain development. Curr. Biol. Published online September 5, 2019. https://doi.org/10.1016/j.cub.2019.07.061.

30. Fachinetti, D., Han, J.S., McMahon, M.A., Ly, P., Abdullah, A., Wong, A.J., and Cleveland, D.W. (2015). DNA sequence-specific binding of CENP-B enhances the fidelity of human centromere function. Dev. Cell *33*, 314–327.

31. Kaulich, M., and Dowdy, S.F. (2015). Combining CRISPR/Cas9 and rAAV templates for efficient gene editing. Nucleic Acid Ther. *25*, 287–296.

32. Ran, F.A., Hsu, P.D., Wright, J., Agarwala, V., Scott, D.A., and Zhang, F. (2013). Genome engineering using the CRISPR-Cas9 system. Nat. Protoc. *8*, 2281–2308.

Figure 4. Loss of Spindle Pole Integrity Contributes to Chromosome Mis-Segregation

(A) Percentage of kinetochores not attached to MTs after the indicated treatment. EBRM ± SD from 2 IEs (>40 cells).

(B) Images of chromosomes in cells treated as indicated. White arrows point to misaligned chromosomes.

(C) Percentage of cells with misalignment chromosomes after the indicated treatment. EBRM ± SD from 3 IEs (>90 cells).

(D) Image of a cell with one MN, indicated by the star.

(E) Percentage of cells with MN after the indicated treatments. EBRM ± SD from 3 IEs (>450 cells).

(F) Stills of RPE-1 CENP-A^{AID}-mCherry H2B after the indicated treatment. White, yellow arrows and star indicate misaligned and polar chromosomes and MN, respectively. Time is in minutes.

(G) Percentage of cells after the indicated treatment in each category. EBRM ± SD from 3 IEs (>50 cells). SSA with unpaired t tests. Scale bars, 5 μm.

(H) Model proposed: (1) in cells with functional centromeres, optimal NDC80 recruitment at kinetochores promotes MTs stability, maintaining mitotic pole integrity. (2) In cells with dysfunctional centromeres, NDC80 recruitment at the kinetochores is strongly reduced, compromising MT stability. (3) Consequently, MT minus-ends are released away from the centrosome, leading to (4) PCM dispersion and (5) displaced centrioles. All these defects are explained by alterations in MT stability, since MT stabilization prevents loss of mitotic pole integrity and (6) partially rescues chromosome mis-segregation defects.

See also Figure S4 and Video S3.

STAR★METHODS

KEY RESOURCES TABLE

REAGENT or RESOURCE	SOURCE	IDENTIFIER
Antibodies		
Guinea pig anti CEP192 antibody (1/500)	Basto lab [29],	N/A
Rabbit Centrin 3 antibody (1/500)	Basto lab [29],	N/A
Mouse anti α-Tubulin antibody (1/500)	Sigma	T9026; RRID:AB_477593
Rabbit anti CEP215 antibody (1/500)	Bethyl Laboratories	A300-554A N/A
Rabbit anti NuMA antibody (1/500)	Novus Biologicals	NB-500-174; RRID:AB_10002562
Mouse anti CENP-A antibody (1/1000)	Abcam	ab13939; RRID:AB_300766
Rabbit anti ASPM antibody (1/500)	Novus Biologicals	NB100-2278; RRID:AB_2060284
Mouse anti γ-Tubulin antibody (1/500)	Sigma	T6557; RRID:AB_477584
Rabbit anti CENP-B antibody (1/500)	Abcam	ab25734; RRID:AB_726801
Goat anti-Rabbit IgG (H+L) Highly Cross-Adsorbed Secondary Antibody, Alexa Fluor 647 (1/250)	ThermoFisher	A21245; RRID:AB_2535813
Goat anti-Guinea Pig IgG (H+L) Highly Cross-Adsorbed Secondary Antibody, Alexa Fluor 488 (1/250)	ThermoFisher	A11073; RRID:AB_253411
Goat anti-Mouse IgG (H+L) Cross-Adsorbed Secondary Antibody, Alexa Fluor 546 (1/250)	ThermoFisher	A11003; RRID:AB_2534071
Rabbit anti CENP-A antibody (1/800)	Cell Signaling	2186S; RRID:AB_2078767
Rabbit anti Katanin A1 antibody (1/1000)	ThermoFisher	PA5-31497; RRID:AB_2548970
Rabbit anti MCAK antibody (1/1000)	Abcam	ab95150; RRID:AB_10675766
Mouse anti Hec1 antibody (1/1000)	Abcam	ab3613; RRID:AB_303949
Rabbit anti CENP-C antibody (1/1000)	a gift from Iain Cheeseman, MIT, Boston and Ben Black, UPENN, Philadelphia	N/A
Mouse anti Vinculin antibody (1/2000)	Sigma	V9264; RRID:AB_10603627
Rabbit anti GAPDH antibody (1/1000)	Cell Signaling	14C10; RRID:AB_561053
Mouse anti CCNB1 antibody (1/1000)	Santa Cruz	sc245; RRID:AB_627338
Goat anti-Rabbit IgG (H+L) Cross-Adsorbed Secondary Antibody, HRP (1/2500)	ThermoFisher	G21234; RRID:AB_2536530
Peroxidase AffiniPure Goat Anti-Mouse IgG (H+L) (1/2500	from Jackson ImmunoResearch	115-035-003; RRID:AB_10015289
Chemicals, Peptides, and Recombinant Proteins		
Dulbecco's modified medium (DMEM) F12	GIBCO	11320-033
Foetal bovine serum (FBS)	GE Healthcare	N/A
Penicillin / streptomycin	GIBCO	15140-122
Dulbecco's modified medium + GlutaMAX	GIBCO	61965-026
Methanol RPE	CARLO ERBA Reagents	414819
16% Paraformaldehyde EM Grade	EMS	15710
Triton X-100	Euromedex	2000-C

(*Continued on next page*)

Continued

REAGENT or RESOURCE	SOURCE	IDENTIFIER
Sodium Azide	Sigma-Aldrich	71289
Oil 10 S, VOLTALEF	VWR Chemicals	N/A
Prolong® Gold antifade reagent supplemented with DAPI	Invitrogen	P36935
BSA	Euromedex	04-100-812-C
β-mercaptoethanol	Bio-Rad	161-0710
Auxin	Sigma	I5148
TAI-1	Selleckchem	S7495
MPI-0479605	Selleckchem	S7488
Taxol	Sigma	T7402
Apcin	Sigma	SML1503
Experimental Models: Cell Lines		
RPE-1 CENP-A^{AID} (female)	[6]	Modified from ATCC Cat# CRL-4000, RRID:CVCL_4388
RPE-1 CENP-A^{AID} mCherry H2B (female)	[6]	Modified from ATCC Cat# CRL-4000, RRID:CVCL_4388
RPE-1 CENP-C^{AID} (female)	This paper	Modified from ATCC Cat# CRL-4000, RRID:CVCL_4388
DLD-1 CENP-A^{AID} (male)	[6]	Modified from ATCC Cat# CCL-221, RRID:CVCL_0248
HeLa CENP-A^{AID} (female)	This paper	Modified from CLS Cat# 300194/p772_HeLa, RRID:CVCL_0030
RPE-1 GFP-CEP192 (female)	Oegema Lab	Modified from ATCC Cat# CRL-4000, RRID:CVCL_4388
Oligonucleotides		
ON-TARGETplus SMARTpool siRNA: siCtrl	Dharmacon	D-001810-10-05
ON-TARGETplus SMARTpool siMCAK	Dharmacon	L-004955-00-0005
ON-TARGETplus SMARTpool siNDC80	Dharmacon	L-004106-00-0005
ON-TARGETplus SMARTpool siKatanin	Dharmacon	L-005157-02-0005
ON-TARGETplus SMARTpool siCCNB1	Dharmacon	L-003206-00-0005
Software and Algorithms		
FiJi	Open Source	https://fiji.sc/RRID:SCR_002285
Prism 7	GraphPad software, Inc. Version 7.0a	https://www.graphpad.com/scientific-software/prism/RRID:SCR_002798
Affinity Designer	Serif	https://affinity.serif.com/fr/designer/RRID:SCR_016952
Illustrator	Adobe Version 2017.0.2	https://www.adobe.com/fr/products/illustrator.html?gclid=Cj0KCQjwyLDpBRCxARIsAEENsrIxneSAr99EbcT1zxLI88fVDfcEAI0lc0ywxaaxoLnKhnvpcNPgym4aAkWrEALw_wcB&sdid=88X75SL1&mv=search&ef_id=Cj0KCQjwyLDpBRCxARIsAEENsrIxneSAr99EbcT1zxLI88fVDfcEAI0lc0ywxaaxoLnKhnvpcNPgym4aAkWrEALw_wcB:G:s&s_kwcid=AL!3085!3!341240860976!e!!g!!illustrator; RRID:SCR_010279
Metamorph	Molecular Devices, USA	https://www.moleculardevices.com/RRID:SCR_002368
Other		
JET PRIME kit	Polyplus Transfection	114-07
NuPAGE Novex 4–12% Bis-Tris pre-cast gels	Life Technologies	NP0321
PVDF transfer membrane	GE	RPN303F
SuperSignal West Pico Chemiluminescent Substrate	Thermo Scientific	34080
Cover glasses, circular, 18 mm	Marienfeld Superior	0111580

LEAD CONTACT AND MATERIAL AVAILABILITY

Further information and requests for resources and reagents should be directed to and will be fulfilled by the Lead Contact, Renata Basto (renata.basto@curie.fr).

This study did not generate new unique reagents.

EXPERIMENTAL MODEL AND SUBJECT DETAILS

Cell culture, generation of cell lines and treatments

Cell culture conditions

Cells were maintained at 37°C in a 5% CO_2 atmosphere. hTERT RPE-1 cells (ATCC Cat# CRL-4000, RRID:CVCL_4388) and HeLa cells (CLS Cat# 300194/p772_HeLa, RRID:CVCL_0030) were grown in Dulbecco's modified medium (DMEM) F12 (11320-033 from GIBCO) containing 10% fetal bovine serum (GE Healthcare), 100 U/mL penicillin, 100 U/mL streptomycin (15140-122 from GIBCO). Flp-In TRex-DLD-1 cells (ATCC Cat# CCL-221, RRID:CVCL_0248) were grown in Dulbecco's modified medium + GlutaMAX (61965-026 from GIBCO) containing 10% fetal bovine serum (GE Healthcare), 100 U/mL penicillin, 100 U/mL streptomycin (15140-122 from GIBCO).

Cellsg were routinely checked for mycoplasma (PlasmoTest-Mycoplasma Detection Kit, InvivoGen, #rep-pt1) and underwent cell authentication by short tandem repeat analysis (powerplex16 HS kit, Promega #DC2101) processed at the Genomics Platform (Department of the translational research, Institut Curie).

Generation of RPE-1 CENP-C^{AID} stable cell line

TALENs were assembled using the Golden Gate cloning strategy and library and cloned into a modified version of pcDNA3.1 (Invitrogen) also containing the Fok I endonuclease domain. TALENs were designed to the C-terminal region of CENP-C gene: GAGGA AAGTGTTCTTC and GGTTGATCTTTCATC. RPE-1 cells were co-transfected with the TALEN expression vectors and the donor cassette (containing the two homology arms for CENP-C C-terminal region and the AID and mRFP gene) by nucleofection (Lonza) using program U-017 and solution KitV (Lonza). Single mRFP-positive cells were then isolated by FACS and tested for efficient CENP-C targeting and depletion by IF.

Generation of HeLa CENP-A^{AID} stable cell line

TALENs were assembled using the Golden Gate cloning strategy and library [30] and cloned into a modified version of pcDNA3.1 (Invitrogen) containing also the Fok I endonuclease domain [30]. TALENs were designed to the N-terminal region of CENP-A gene: GTCATGGGCCCGCGCC and GGCCCCGAGGAGGCGCA. HeLa cells were co-transfected with the TALEN expression vectors and the donor cassette (containing the two homology arms for CENP-A N-terminal region and the AID and EYFP gene) by nucleofection (Lonza) and positive clones were selected by FACS.

Generation of RPE-1 GFP-CEP192 cell line

RPE-1 CEP192-NeonGreen cells were generated by using CRISPR/Cas9 technology in combination with rAAV mediated delivery of the repair construct [31]. The gRNA was designed to cut close to the stop codon of CEP192 (CGACTAATTGGTGAAGCTCT) and cloned into PX459 [32], a gift from Feng Zhang (Addgene plasmid # 48139; http://addgene.org/48139; RRID:Addgene_48139). The repair construct was cloned into pSEPT and contains the left and right flanking region of the gRNA target site (960 bp and 672 bp). NeonGreen, for C-terminal fusion to CEP192, and the neomycin resistance gene aminoglycoside phosphotransferase from Tn5 was cloned between the left and right homology arms. The expression of the neomycin resistance gene is linked to endogenous CEP192-NeonGreen expression through a P2A sequence.

Treatments

The following drugs are used in this study (the concentrations are indicated in the figures):

500μM Auxin (Sigma; I5148). TAI-1 (Selleckchem, S7495). Taxol (Sigma, T7402). Apcin (Sigma, SML1503). MPI-0479605 (Selleckchem, S7488).

METHOD DETAILS

Immunofluorescence microscopy

Cells were plated on coverslips in 12-well plates and treated with the indicated drugs. The day of the immunofluorescence, cells were fixed using cold methanol (7 min at −20°C) or for NuMA and ASPM staining with 4% of paraformaldehyde + Triton X-100 (2000-C from Euromedex) 0,1% in PBS (20 min at RT). Then, cells were washed three times using PBS-T (PBS 1X + 0,1% Triton X-100 + 0,02% Sodium Azide) and incubated with PBS-T + BSA (04-100-812-C from Euromedex) 0,5% during 30 min at RT. After three washes with PBS-T, primary and secondary antibodies were incubated in PBS-T + BSA 0,5% during 1 hr and 30 min at RT, respectively. Nuclear DNA was detected by mounting slides in Prolong® Gold antifade reagent supplemented with DAPI (P36935 from Invitrogen).

For super-resolution microscopy

Images were acquired on a spinning disk microscope (Gataca Systems, France). Based on a CSU-W1 (Yokogawa, Japan), the spinning head was mounted on an inverted Eclipse Ti2 microscope equipped with a motorized XY Stage (Nikon, Japan). Images were acquired through a 100x 1.4NA Plan-Apo objective with a sCMOS camera (Prime95B, Photometrics, USA). Optical sectioning

was achieved using a piezo stage (Nano-z series, Mad City Lab, USA). Gataca Systems' laser bench was equipped with 405, 491 and 561 nm laser diodes, delivering 150 mW each, coupled to the spinning disk head through a single mode fiber. Multi-dimensional acquisitions were performed using Metamorph 7.10.1 software (Molecular Devices, USA). Super resolution was achieved on the CSU-W1 spinning disk equipped with a super-resolution module (Live-SR, Gataca systems). This module is based on structured illumination with optical reassignment technique and online processing leading to a two-time resolution improvement. The method called multifocal SIM (MSIM) allows combining the doubling resolution together with the physical optical sectioning of confocal microscopy.

For classical microscopy

Images were acquired on an upright widefield microscope (DM6B, Leica Systems, Germany) equipped with a motorized XY and a 100X objective (HCX PL APO 100X/1,40-0,70 Oil from Leica). Acquisitions were performed using Metamorph software (Molecular Devices, USA) and a sCMOS camera (Flash 4V2, Hamamatsu, Japan).

Stacks of conventional fluorescence images were collected automatically at a Z-distance of 0.2 μm (Metamorph software; Molecular Devices, RRID:SCR_002368). Images are presented as maximum intensity projections generated with ImageJ software (RRID:SCR_002285), from stacks deconvolved with an extension of Metamorph software (RRID:SCR_002368).

Primary and secondary antibodies were used at the following concentrations

Primary antibodies: Guinea pig anti CEP192 antibody (1/500; Basto lab [29]), Rabbit Centrin 3 antibody (1/500; Basto lab [29]), Mouse anti Tubulin antibody (1/500; T9026 from Sigma, RRID:AB_477593), Rabbit anti CEP215 antibody (1/500; A300-554A from Bethyl Laboratories); Rabbit anti NuMA antibody (1/500; NB-500-174 from Novus Biologicals, RRID:AB_10002562); Mouse anti CENP-A antibody (1/1000; ab13939 from Abcam, RRID:AB_300766), Rabbit anti ASPM antibody (1/500; NB100-2278 from Novus Biologicals, RRID:AB_2060284), Mouse anti γ-Tubulin antibody (1/500; T6557 from Sigma, RRID:AB_477584), Rabbit anti CENP-B antibody (1/500; ab25734 from Abcam, RRID:AB_726801), Goat anti-Rabbit IgG (H+L) Highly Cross-Adsorbed Secondary Antibody, Alexa Fluor 647 (1/250; A21245 from ThermoFisher, RRID:AB_2535813), Goat anti-Guinea Pig IgG (H+L) Highly Cross-Adsorbed Secondary Antibody, Alexa Fluor 488 (1/250; A11073 from ThermoFisher, RRID:AB_253411), Goat anti-Mouse IgG (H+L) Cross-Adsorbed Secondary Antibody, Alexa Fluor 546 (1/250; A11003 from ThermoFisher, RRID:AB_2534071).

Live imaging

Cells were plated on a dish (FD35-100 FluoroDish from World Precision Instruments) and treated with the indicated drug/siRNA or transfected with GFP-EB1 plasmid (a gift from Lynne Cassimeris / Addgene plasmid #17234 [14],). Images were acquired on a spinning disk microscope (Gataca Systems, France). Based on a CSU-W1 (Yokogawa, Japan), the spinning head was mounted on an inverted Eclipse Ti2 microscope equipped with a motorized XY Stage (Nikon, Japan). Images were acquired through a 40x 1.4NA Plan-Apo objective with a sCMOS camera (Prime95B, Photometrics, USA). Optical sectioning was achieved using a piezo stage (Nano-z series, Mad City Lab, USA). Gataca Systems' laser bench was equipped with 405, 491 and 561 nm laser diodes, delivering 150 mW each, coupled to the spinning disk head through a single mode fiber. Multi-dimensional acquisitions were performed using Metamorph 7.10.1 software (Molecular Devices, USA). Stacks of conventional fluorescence images were collected automatically at a Z-distance of 1.5 μm (Metamorph software; Molecular Devices, RRID:SCR_002368). Images are presented as maximum intensity projections generated with ImageJ software (RRID:SCR_002285), from stacks deconvolved with an extension of Metamorph software (RRID:SCR_002368).

Cold treatment

Cells were plated on coverslips in 12-well plates and treated with the indicated drugs. The day of the immunofluorescence, cells were incubated during 12 min on ice and then incubated 30 s with Microtubule buffer (100 mM Pipes pH 6.9 with KOH, 0.1 mM CaCl2, 1 mM MgCl2, 0.1% Triton X-100). After, cells were fixed using 4% of paraformaldehyde in Microtubule buffer (25 min at RT). Then, cells were washed three times using PBS-T (PBS 1X + 0,1% Triton X-100 + 0,02% Sodium Azide) and incubated with PBS-T + BSA 0,5% during 1 hr at RT. After three washes with PBS-T, primary and secondary antibodies were incubated in PBS-T + BSA 0,5% during 1 hr and 30 min at RT, respectively. Nuclear DNA was detected by mounting slides in Prolong® Gold antifade reagent supplemented with DAPI (P36935 from Invitrogen). For super-resolution microscopy, images were acquired on a spinning disk system (Gataca Systems, France) based on an inverted microscope (Ti-E, Nikon) equipped with a sCMOS camera (Prime 95B, Photometrics), a confocal spinning head (X1, Yokogawa), a 100x 1.4 NA Plan Apo objective lens and a super-resolution module (Live-SR, Gataca systems) based on structured illumination with optical reassignment technique and online processing leading to a two-time resolution improvement. The method called multifocal SIM (MSIM) allows combining the doubling resolution together with the physical optical sectioning of confocal microscopy. Stacks of conventional fluorescence images were collected automatically at a Z-distance of 0.2 μm (Metamorph software; Molecular Devices, RRID:SCR_002368). Images are presented as maximum intensity projections generated with ImageJ software (RRID:SCR_002285), from stacks deconvolved with an extension of Metamorph software (RRID:SCR_002368).

siRNA transfection

siRNAs were provided by Dharmacon (ON-TARGETplus SMARTpool siRNA: siCtrl D-001810-10-05; siMCAK L-004955-00-0005; siNDC80 L-004106-00-0005, siKATNA1 L-005157-02-0005, siCCNB1 L-003206-00-0005) and were used at 50 nM. Cells were

transfected during 72 hr using JET PRIME kit (Polyplus Transfection, 114-07) according to the manufacturer protocol and 24 hr before the end of the transfection cells were left untreated or treated with Auxin or TAI-1.

Western Blot analysis and antibodies

Cells were lysed in 8 M urea, 50 mM Tris HCl, pH 7.5 and 150 mM β-mercaptoethanol (161-0710 from Bio-Rad), sonicated and heated at 95°C for 10 min. Samples (equivalent of 2 × 10^5 cells) were subjected to electrophoresis in NuPAGE Novex 4%–12% Bis-Tris pre-cast gels (NP0321 from Life Technologies). Protein fractions from the gel were electrophoretically transferred to PVDF membranes (PVDF transfer membrane; RPN303F from GE). After 1chr saturation in PBS containing 5% dry non-fat milk and 0.5% Tween 20, the membranes were incubated for 1chr with primary antibody (*see below*) diluted in PBS containing 5% dry non-fat milk and 0.5% Tween 20. After three 10 min washes with PBS containing 0.5% Tween 20, the membranes were incubated for 45cmin with a 1/2c500 dilution of peroxidase-conjugated antibody (*see below*). Membranes were then washed three times with PBS containing 0.5% Tween 20, and the reaction was developed according to the manufacturer's specifications using ECL reagent (SuperSignal West Pico Chemiluminescent Substrate; 34080 from Thermo Scientific).

Primary and secondary antibodies were used at the following concentrations

Rabbit anti CENP-A antibody (1/800; 2186S from Cell Signaling, RRID:AB_2078767), Mouse anti Tubulin (1/5000; T9026 from Sigma, RRID:AB_477593), Rabbit anti Katanin A1 antibody (1/1000; PA5-31497 from ThermoFisher, RRID:AB_2548970), Rabbit anti MCAK antibody (1/1000; ab95150 from Abcam, RRID:AB_10675766), Mouse anti Hec1 antibody (1/1000; ab3613 from Abcam, RRID:AB_303949). Rabbit anti CENP-C antibody (1/1000; a gift from Iain Cheeseman, MIT, Boston and Ben Black, UPENN, Philadelphia), Mouse anti Vinculin antibody (1/2000, V9264 from Sigma, RRID:AB_10603627), Rabbit anti GAPDH antibody (1/1000; 14C10 from Cell Signaling, RRID:AB_561053), Mouse anti CCNB1 antibody (1/1000; sc245 from Santa Cruz, RRID:AB_627338), Goat anti-Rabbit IgG (H+L) Cross-Adsorbed Secondary Antibody, HRP (1/2500; G21234 from ThermoFisher, RRID:AB_2536530), Peroxidase AffiniPure Goat Anti-Mouse IgG (H+L) (1/2500; 115-035-003 from Jackson ImmunoResearch, RRID:AB_10015289).

Chromosome spreads for cohesion defect analysis

Cells were grown to ~75%–80% confluency and growth medium was collected together with washing solution (1X PBS) and used to harvest mitotic cells after trypsinisation. Cells were centrifuged 5 min at 900 rpm. Pellet was gently resuspended in 5 mL of hypotonic solution (75 mM KCl) and cells were incubated for 15 min at 37°C. One mL of Carnoy's fixative solution (methanol: acetic acid, 3:1) was added and cells were centrifuged (5 min, 900 rpm). Pellet was resuspended in 5 mL of Carnoy's added drop by drop on a low speed vortex and cells were fixed 30 min at RT before centrifugation. Supernatant was discarded leaving a sufficient volume of carnoy's to resuspend the pellet. Cells were spread onto a cold glass slide and let dry. Slides were mounted using DAPI antifade (metasystems probes). Immunofluorescence images were collected using a Deltavision Core system (Applied Precision).

QUANTIFICATION AND STATISTICAL ANALYSIS

Quantifications

Image analysis and quantifications were performed using ImageJ software. MT minus-end and PCM areas have been quantified using "wand" tool from ImageJ software. Angle between pole-to-pole axis and centrioles (angle α) has been measure using "angle" tool from ImageJ software.

Statistical analysis

At least three (n) independent experiments were carried out to generate each dataset. All data underwent normality check (Shapiro-Wilk test) and in respect to that, appropriate tests were performed. Student's t test was used to compare two conditions. Kruskal-Wallis test was used to compare two populations. Fisher's exact test was used to evaluate association between parameters.

Differences were considered statistically significant at values of Pc $\leq$ c0.05. These tests were performed using GraphPad Prism (RRID:SCR_002798) version 7.00 for Mac, GraphPad Software, La Jolla California USA, https://www.graphpad.com.

DATA AND CODE AVAILABILITY

This study did not generate/analyze datasets or code.